Oxygen ordering in untwinned YBa₂Cu₃O₇₋δ films driven by electrothermal stress

Stefan Marinković [1,*] Edoardo Trabaldo,[2] Simon Collienne [1,†] Floriana Lombardi,[2]
Thilo Bauch,[2,‡] and Alejandro V. Silhanek [1,§]

[1]*Experimental Physics of Nanostructured Materials, Q-MAT, CESAM, Université de Liège, B-4000 Sart Tilman, Belgium*
[2]*Department of Microtechnology and Nanoscience, Quantum Device Physics Laboratory,
Chalmers University of Technology, SE-41296 Göteborg, Sweden*

We experimentally investigate the displacement of oxygen vacancies at high current densities in highly untwinned YBa₂Cu₃O₇₋δ films grown on top of MgO substrates. Transport bridges oriented along the YBa₂Cu₃O₇₋δ crystallographic directions [100] (*a* axis), [010] (*b* axis), and [110] (45° from principal axes) reveal that the onset of vacancy migration is mainly determined by the local temperature (or equivalently by the dissipated power) rather than the associated activation energy. Exceeding this threshold value, a clear directional migration proceeds as evidenced by optical microscopy. Concomitant electrotransport measurements show that an intermediate phase, characterized by a decrease in resistivity, precedes long-range migration of vacancies. We numerically demonstrate that this intermediate phase consists of a homogenization of the oxygen distribution along the transport bridge, a phenomenon strongly dependent on the activation energy and the initial degree of disorder. These findings provide some important clues to determine the level of order/disorder in YBa₂Cu₃O₇₋δ films based on electric transport measurements.

I. INTRODUCTION

There is currently a renewed interest in the targeted manipulation of oxygen atoms and vacancies in oxide films fueled by the perspective of promising potential applications including bipolar nonvolatile resistive switches [1], all-electrical doping of cuprates [2,3], electrically driven redox reaction [4], ionic conductors for fuel cell technology [5,6], or fine-tuning properties of high-temperature superconducting quantum interferometers [7]. In particular, the possibility to induce oxygen motion via electromigration (EM) in electron-doped [8] as well as hole-doped [9] superconducting cuprates and ferromagnetic manganites La₀.₇Sr₀.₃MnO₃ [10] has been recently demonstrated, pointing towards a universal phenomena touching a broad spectrum of other complex oxides, such as nickelates and cobaltates. The rich variety of electronic phases exhibited by these materials as a function of oxygen content could to some extent be reversibly probed in the very same sample by just exposing it to large current densities or electric fields. This has been demonstrated for YBa₂Cu₃O₇₋δ in Refs. [9,11].

These studies have been performed on nonuniform crystallographically oriented samples which are polluted by twin boundaries regularly exchanging the *a*- and *b*-crystal axes. This condition masks the fact that oxygen diffusion is expected to be largely favored along the *b* than along the *a* axis. In other words, the activation energy E_a associated with oxygen migration should be strongly dependent on the in-plane

direction. Thus far, little is known about the influence of an anisotropic activation energy on the migration phenomenon.

In this paper, we address this question by investigating the current-stimulated oxygen migration process in 80% untwinned films with electric current flowing along different in-plane crystallographic orientations. The preferential alignment of the CuO chains along one of the in-plane directions of the substrate results from the large mismatch between the MgO substrate and the YBCO layer [12]. There are two competing mechanisms determining the onset of electromigration. On one hand, the activation energy is lower along *b*, thus, favoring oxygen diffusion in that direction. On the other hand, migration onset is a thermally activated process triggered by Joule heating first along the *a* direction due to its higher resistivity. We demonstrate that the latter effect sets the onset of electromigration, whereas clear hints of an anisotropic activation energy are seen in the propagation of the oxygen depleted front as well as in the degree of average oxygen ordering induced by the current. Finite elements modeling provide further insights permitting to link the electrotransport measurements with real-space oxygen distribution maps.

II. METHODS

A. Experimental details

Epitaxial 50-nm-thick YBa₂Cu₃O₇₋δ films were grown by pulsed laser deposition with the *c* axis aligned perpendicular to the film plane on MgO(110) single-crystal substrates. For ensuring ohmic electrical contacts, Au electrodes were sputtered. The films were patterned via electron-beam lithography [13,14] and dry ion-beam etching into bridge-type constrictions as shown in Fig. 1. The length × width of the bridges is 5×2 µm². All films exhibited superconducting

*smarinkovic@uliege.be
†scollienne@uliege.be
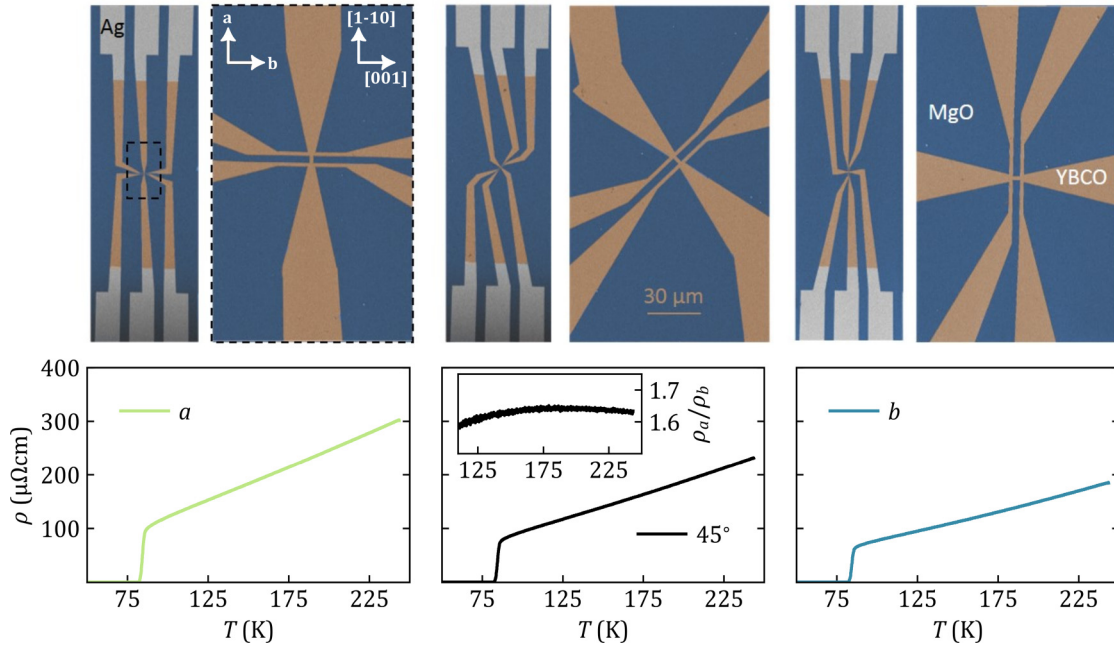‡bauch@chalmers.se
§asilhanek@uliege.be

FIG. 1. Low magnification and high magnification false-colored scanning electron microscopy images of transport bridges along the crystallographic directions a (left), $45°$ from a (top central panel), and b (rightmost panel). The lower row shows the associated resistivity vs temperature curves obtained at zero applied magnetic field. The inset in the lower central panel shows the ratio ρ_a/ρ_b as a function of temperature in the normal state.

critical temperatures $T_c \sim 87.5$ K (corresponding to doping $p \sim 0.19$). The asymmetrical (038)–(308) reflections in 2θ-ω x-ray diffraction (XRD) maps reveal a 80% untwinning degree [12]. The measurements presented in this paper have been tested in four full sets of samples (i.e., 12 bridges in total).

The optical microscopy images were obtained under atmospheric conditions with a $50\times$ magnification objective (numerical aperture$= 0.5$) followed by a $2\times$ magnification lens and collected in bright-field mode with a continuous green illumination filtered from a Hg lamp. The optical microscopy imaging is performed simultaneously with the electrotransport in order to be able to make a reliable comparison of the electromigration effects.

B. Finite elements modeling

The model considers the YBCO sample as a continuous material whose state can vary locally between tetragonal or orthorhombic configurations corresponding to oxygen concentration c between $c_{\min} = 3.41 \times 10^{28}$ and $c_{\max} = 4.01 \times 10^{28}$ ions m^{-3}, respectively [15]. We further assume that only the oxygen in excess to the tetragonal state can contribute to the oxygen diffusion [1] and define the adimensional variable $x = (c - c_{\min})/(c_{\max} - c_{\min})$ to distinguish between insulating ($x = 0$) and superconducting ($x = 1$) states. It is assumed that the temporal evolution of x is governed by Eq. (1). The first term on the right-hand side represents a conventional diffusion process due to an inhomogeneous distribution of oxygen whereas the second term comes from the combined effect of electron wind and electric field as a consequence of an applied voltage V,

$$\frac{\partial x}{\partial t} = \nabla(\mathbf{D} \cdot \nabla x + z\mathbf{u}Fx\nabla V), \qquad (1)$$

with $\mathbf{D} = D_0\text{diag}[\exp(-E_{a_a}/k_BT), \exp(-E_{a_b}/k_BT)]$ the temperature-dependent diffusion tensor, $D_0 = 1.4 \times 10^{-8}$ m^2 s^{-1} [16], E_{a_a} and E_{a_b} the activation energies in eV along directions a and b, respectively, k_B is the Boltzmann constant, z is the charge number of oxygen ions, $\mathbf{u}$ is the Nernst-Einstein ratio ($\mathbf{u} = \mathbf{D}/RT$), and F is the Faraday number. In addition, the heat equation,

$$\rho_m C\frac{\partial T}{\partial t} = \kappa\nabla^2 T + \boldsymbol{\rho}(x, T)\mathbf{J}^2 \qquad (2)$$

is solved in order to obtain the spatial distribution of temperature T, where ρ_m is the density in kg m^{-3}, C the specific-heat capacity in J kg^{-1} K^{-1}, T the temperature in K, κ is the thermal conductivity in W K^{-1} m^{-1}. The second term on the right-hand side of equation (2) represents the Joule heating and involves the resistivity tensor $\boldsymbol{\rho}(x, T) = \text{diag}[\rho_a, \rho_b]$ of the material which depends on both the oxygen concentration and local temperature. The ratio $\rho_a(x_0, T_{\text{ref}})/\rho_b(x_0, T_{\text{ref}}) = 380/236$ at the initial oxygen concentration x_0 is determined from measurements at low current (see Fig. 2). The functionality $\boldsymbol{\rho}(x, T)$ imposed in the model is taken from experimental values reported in Ref. [17]. For $T > 300$ K, we assume a linear-dependent resistivity $\boldsymbol{\rho}(x, T) = [1 + \alpha(T - T_{\text{ref}})]\boldsymbol{\rho}(x, T_{\text{ref}})$ with $\alpha = 5 \times 10^{-3}$ K^{-1} determined by $R(T)$ measurements and $T_{\text{ref}} = 300$ K.

Finally, the Poisson equation is solved to obtain the electric potential distribution in the sample with the conductivity $\boldsymbol{\sigma} = \text{diag}[\rho_a^{-1}, \rho_b^{-1}]$,

$$\nabla \cdot (\boldsymbol{\sigma}\nabla V) = 0. \qquad (3)$$

Note that the right-hand term of Eq. (3) is set to zero in order to guarantee charge neutrality throughout the device. The electric field $\mathbf{E} = -\nabla V$ is related to the current density $\mathbf{J}$
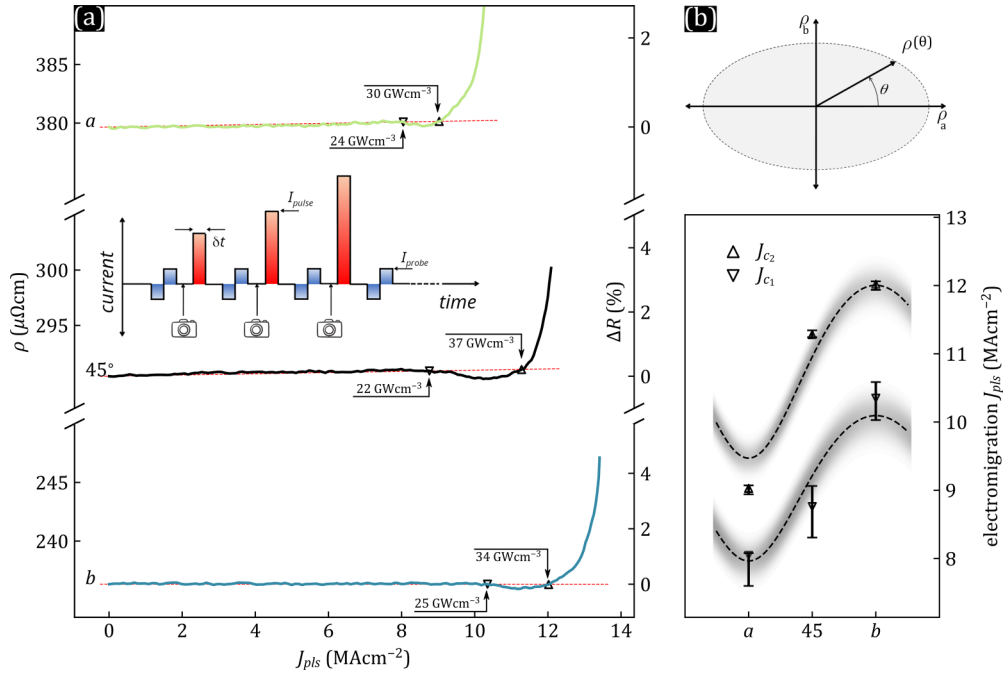
FIG. 2. (a) Evolution of the sample resistivity as a function of the applied pulsed current density for bridges oriented along three crystallographic axes. The power dissipated in the bridges at the onset of the resistivity decrease (∇) and increase ($\triangle$), is indicated with black arrows. The inset shows the measurement protocol using pump-probe current pulses and intercalated optical microscopy snapshots. (b) Schematic of the anisotropic $\rho(\theta)$ following an elliptic angular dependence (upper panel). The lower panel shows the experimentally determined onset of the sample resistivity decrease (∇) and the increase ($\triangle$). The gray shadow covers a zone limited by the fittings to Eq. (4) for the extreme (minimum and maximum) power p_0 inferred from the experimental data points.

by Ohm's constitutive equation $\mathbf{J} = \sigma \mathbf{E}$ and does not take into account the ionic current whose contribution is negligible [1]. We will first consider an isotropic version of the equations that satisfactorily explains the electrotransport properties and later on add a slight anisotropy of the oxygen diffusion in order to better account for the observed oxygen vacancy mappings. The solution of the system of Eqs. (1)–(3) with proper boundary conditions is obtained for the exact geometry of the real sample using the finite element software COMSOL [18]. Due to the small thickness/width aspect ratio, a two-dimensional version of Eqs. (1)–(3) is solved for the YBCO layer whereas only Eq. (2) is solved for the substrate. The values of the thermal coefficients are listed in Table I. Slightly different thermal coefficients as reported in Refs. [19,20] lead to similar results.

Having a system of coupled equations combined with logarithmic behavior of resistivity with concentration makes simultaneous resolution particularly demanding. In order to speed up the numerical calculations, an iterative time process with two steps per iteration is used [26]. First, the temperature and potential profiles are evaluated at iteration i assuming x

to be constant as determined in the previous iteration $i - 1$. During this step, the temperature dependence of the resistivity is assumed to be the temperature profile from the previous iteration. Second, the new spatial distribution of the concentration x is calculated assuming T and V are constant. The values T, V, and x at the first iteration are given by the initial conditions of the problem.

III. EXPERIMENTAL RESULTS: DC ELECTROMIGRATION

Early investigations of oxygen tracer diffusion in untwinned single-crystalline YBCO showed that the oxygen diffusion along the b direction (the direction of the CuO chains) can be substantially faster than diffusion along the a direction [27]. This fact suggests the possibility to achieve current-induced oxygen migration more easily if the transport bridge is oriented along the b axis than along the a axis. (See Ref. [26] and references therein). In order to address this question, we have fabricated transport bridges oriented along three crystallographic directions, namely, [100] [a in Fig. 1(a)], [110] [45° off a in Fig. 1(b)], and [010] [b in Fig. 1(c)]. The lower row in Fig. 1 shows the corresponding resistivity vs temperature response obtained at zero applied magnetic field. The fact that the resistivity along the b axis is the lowest comes from the fact that CuO chains aligned along this direction provide an extra conductive channel absent along the a direction. Friedmann *et al.* [28] reported a ratio $\rho_a/\rho_b \approx 2.2 \pm 0.2$ for untwinned single crystals in a broad temperature range. Assuming a similar value for a

TABLE I. Thermal coefficients for the MgO substrate and the superconducting YBCO film used as input parameters in COMSOL simulations.

	ρ_m (kg m^{-3})	C (J kg^{-1} K^{-1})	κ (W K^{-1} m^{-1})
MgO	3600 [21]	930 [21]	50 [21]
YBCO	6300 [22,23]	520 [24,25]	10 [25]

perfectly (100%) untwinned thin film and considering that in our samples $\rho_a/\rho_b \approx 1.6$ (see the inset in the lower rightmost panel), we estimate a $75 \pm 5\%$ untwinning within a linear approximation. This indirect estimation is consistent with the more direct XRD measurements but is somewhat less accurate due to the influence of anisotropic stress imposed to the atomic lattice by the substrate.

The protocol used to achieve electrically stimulated oxygen migration consists of applying 1-s pulses of DC current with linearly increasing amplitude [see the inset in Fig. 2(a)]. The resistance of the sample is probed after every driving pulse with a small bipolar pulse of 10 μA (0.001 MA cm^{-2}) amplitude and 10-s duration. Samples are optically imaged after the resistance measurement is finished, once for every amplitude of the driving pulse. This experiment is performed under atmospheric conditions. Figure 2(a) shows the resulting evolution of the bridge resistivity as a function of the density of current during the electric pulse. Pulses of small amplitude lead to no modification of the sample resistance as manifested by the current independent resistivity. Beyond a certain threshold current density, a slight decrease in resistivity (less than 1%) is systematically observed. As demonstrated by Moeckly *et al.* [29] this effect cannot be solely attributed to a thermal annealing process resulting from Joule heating but requires in addition, a current stimulated redistribution of chain oxygen vacancies. Interestingly, this improvement of the conductive properties is less pronounced when the current is along the a axis which is consistent with the fact that oxygen diffusion (and, thus, ordering) is hampered along this direction. This initial improvement of the sample is followed by a rapid increase in the resistivity associated with long-range oxygen migration. Remarkably, even though the activation barrier is expected to be substantially lower for oxygen diffusion along the b axis, the current density needed to stimulate the diffusion process is larger along b than along a. The reason for this effect can be traced back to the fact that for a given current, a higher resistivity along a implies a more pronounced Joule heating and, consequently, a higher local temperature. Since oxygen migration is thermally activated, this effect gives rise to an early oxygen diffusion along a as current density increases.

A possible way to discern thermally driven from electrically induced oxygen displacement is to compare the power dissipated at the onset of migration. Indeed, for an isotropic system for which the diffusivity does not depend on the in-plane direction, the diffusion should be triggered at the same temperature (proportional to the power applied) independently of the direction of the current. In other words, the onset of migration should take place at a constant power threshold for all in-plane current orientations. In Fig. 2(a) we indicate the power density $\mathfrak{P} = \rho J^2$ at the onset of resistivity decrease as well as at the onset of resistivity increase for the three investigated current directions. The fact that $\mathfrak{P}$ at the onset of resistivity decrease is nearly independent of the orientation suggests that the threshold for electromigration is determined by the local temperature rather than the activation energy. Indeed, for a given current, in the expression for diffusivity $D \propto \exp(-E_a/k_B T)$, the local temperature $T \propto \rho$. Both E_a and ρ are highest along the a axis, and these two parameters have competing ef-
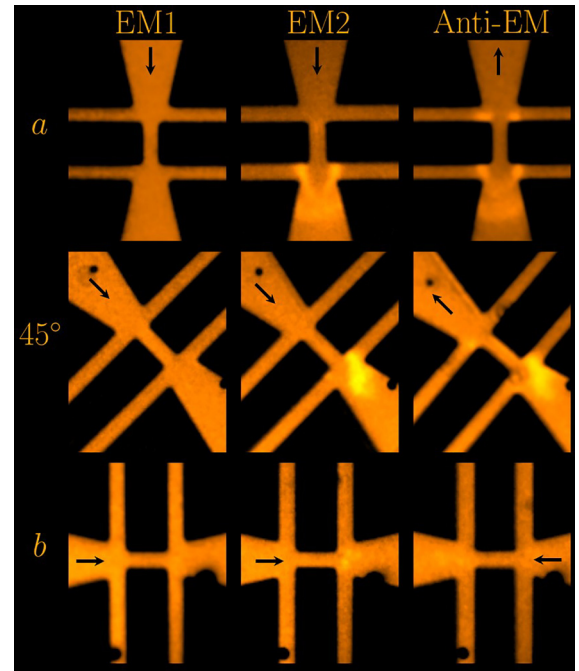

FIG. 3. Bright-field optical microscopy images for the bridges oriented along a, 45°, and b crystallographic directions after (EM1) mild electromigration with $\sim 3\%$ increase in resistance, (EM2) severe electromigration with $\sim 30\%$ increase in resistance, and (anti-EM) reversing the current polarity, so-called antielectromigration. All the images were acquired on the same sample in chronological order EM1, EM2, and finally anti-EM under ambient conditions. The black arrows indicate the current direction.

fects. If the angular variation of ρ is more pronounced than that of E_a, a minimum in the threshold current density for electromigration is expected along the a axis, as observed experimentally.

Assuming that the onset of electromigration is defined by a power density threshold p_0 and considering an anisotropic resistivity $\rho(\theta)$ of elliptic shape as schematically shown in the upper panel of Fig. 2(b), it is possible to deduce a current density threshold of electromigration,

$$j(\theta) = \sqrt{\frac{p_0}{\rho_a \rho_b}} \sqrt{(\rho_a \sin \theta)^2 + (\rho_b \cos \theta)^2}. \tag{4}$$

The lower panel of Fig. 2(b) shows the experimentally determined onset of the sample resistivity decrease ($\bigtriangledown$) and the onset of sample resistivity increase ($\bigtriangleup$) together with the prediction of Eq. (4) with a graded color intensity representing the error bar on p_0. The fair agreement between the proposed model and the experimental data validates the scenario for which the electromigration onset is set by the local power density or, equivalently, by the local temperature.

In Fig. 2 we have purposely limited the irreversible increase of resistivity to few percent of the initial value. After this first electromigration, no hint of sample modifications were observed by optical reflectivity. However, by further increasing the current density in such a way to induce $\sim 30\%$ increase in resistance, the oxygen-deficient regions become visible by optical microscopy [30]. Figure 3 shows a selected set of snapshots of the diffusion process in which affected

areas exhibit a higher reflectivity (i.e., brighter color). These images point to the existence of oxygen depleted spots at the sharp corners of the structure and propagating into the current leads, suggesting the importance of current crowding in the triggering process. Similar findings were recently reported for fully twinned YBCO films on LaAlO$_3$ substrates [9,26]. No major changes are observed on the central bridge itself. Note that the diffusion pattern observed along the a and b axes is symmetric, whereas, the one observed along 45° is asymmetric, suggestive of an influence of the crystallographic orientation. Nevertheless, the affected area is clearly directional demonstrating the electric current/field drive on the displacement of atoms. Based on the above considerations, we suggests a scenario in which the onset of electromigration is dictated by the local temperature at the transport bridge, and the direction of electromigration is determined by the applied electric field and/or current density.

Attempts to recover the initial resistance of the bridges by reversing the current polarity have proven unsuccessful unless the resistance changes are within a few percent of the starting resistance. Transport measurements show that a minor healing effect takes place before a new increase in resistance develops. This minor healing process is also visible in the rightmost column of Fig. 3 (labeled anti-EM) as the brightness of the oxygen depleted area decreases whereas new white spots appear on the opposite side of the bridge.

IV. NUMERICAL SIMULATIONS: DC ELECTROMIGRATION

Let us now investigate the oxygen diffusion process by following the numerical model introduced above and considering the same exact geometry as for the sample investigated experimentally. Our first objective consists in demonstrating that the onset of electromigration is entirely determined by the power density and the local temperature, rather than the current density. To that end, we will assume that the activation energy for oxygen diffusion $E_{a_a} = E_{a_b} = E_a$ are independent of the crystallographic orientation, whereas, the homogeneous resistivity ρ changing with angle as shown in Fig. 2(b) is considered.

Figure 4(a) shows the resistance as a function of the applied current for an ensemble of bridges with identical shape but different resistivity. The simulation parameters have been chosen in such a way to approach the experimental data shown in Fig. 2(a). The current threshold for electromigration determined using a 1% increase in resistance is plotted in Fig. 4(b) as a function of the sample's resistivity. In the same panel the experimental data have been added and show a similar trend as for the simulation, i.e., the current threshold for electromigration decreases as resistivity increases. Simulations allow us to estimate the maximum temperature T_{max} attained at the onset of electromigration as shown in the inset of panel (b) for each of the curves in panel (a). One can observe that the local temperature triggering the oxygen migration process is rather independent of the sample resistivity, thus, confirming that T_{max} is the essential parameter controlling the onset of the migration process. In the same inset we have plotted the power delivered at the bridge at the onset of electromigration
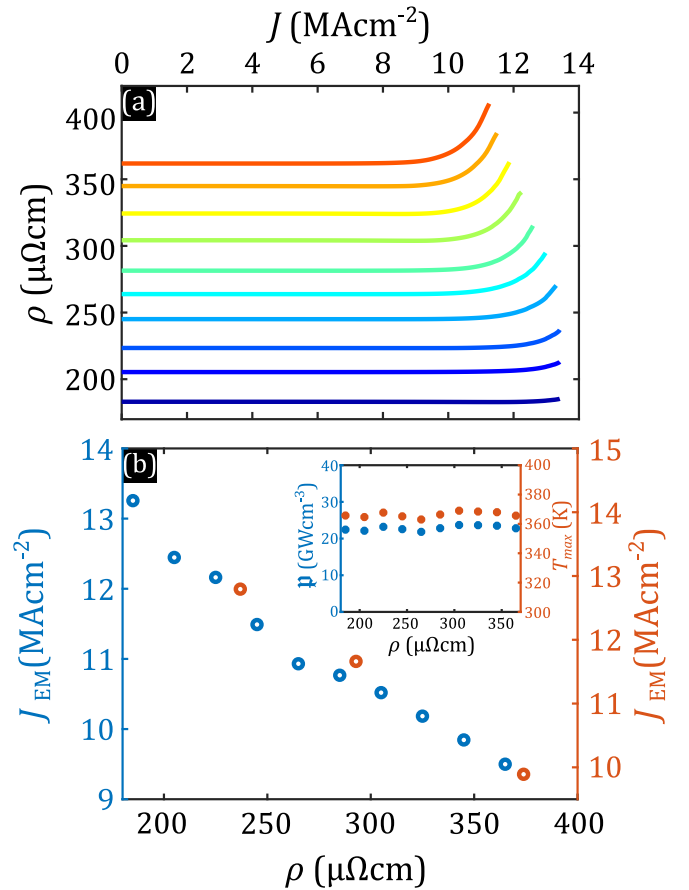

FIG. 4. (a) Numerical simulation of the sample resistance for ρ varying from 185 to 365 $\mu\Omega$ cm in steps of 20 $\mu\Omega$ cm. The following parameters have been used for these simulations: $E_a = 0.55$ eV, $\alpha = 5 \times 10^{-3}$ K^{-1}, $x_0 = 0.9$, $\delta x_0 = 5\%$, $x_{min} = 0.5$, and $x_{max} = 0.95$. (b) Electromigration current determined using a criterion of a 1% increase on resistance as a function of the resistivity extracted from the numerical simulation (blue) and the experiments (orange). The inset shows the power density (left ordinate) and maximum temperature (right ordinate) at the onset of electromigration for samples of different resistivities.

and, as expected, it shows a similar trend as T_{max}. In brief, the experimental trend shown in Fig. 2(b) can be simply accounted for by an increase in resistivity without the need to invoke an angular-dependent E_a.

Interestingly, as shown by the blue curve in Fig. 5(a), the proposed numerical model is also able to capture the experimentally observed improvement of the conductive properties of the bridges in the vicinity of the onset of electromigration as seen in Fig. 2(a). In order to demonstrate that the origin of this resistance shallow minimum can be linked to the ordering or homogenization of the oxygen concentration, we computed the residual r defined by

$$r = \sum_i \sqrt{(x_i - x_0)^2}, \qquad (5)$$

with i indicating each node of the simulation grid, x_i indicating the local oxygen concentration, and x_0 indicating the mean value of the concentration throughout the sample. In other words, $\delta x_i = x_i - x_0$ and r represent the degree of local and
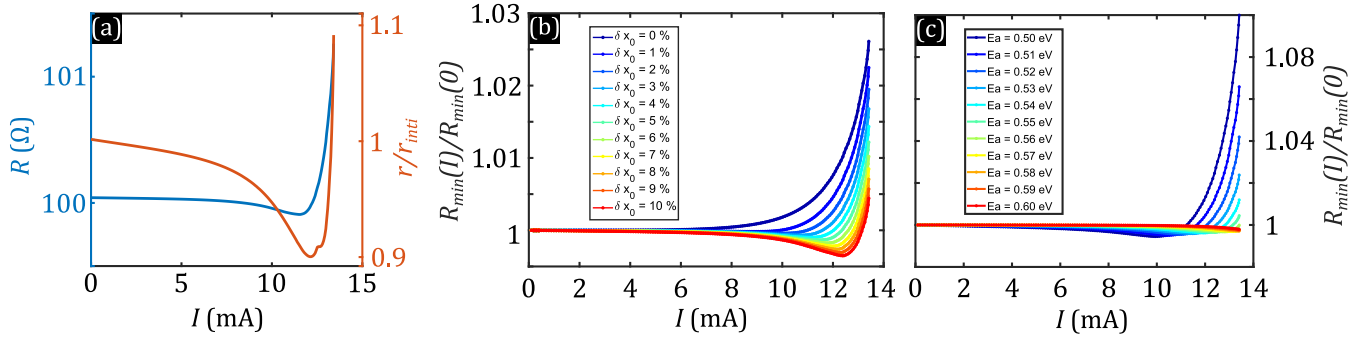
FIG. 5. (a) Zoom in showing the numerically calculated initial change in resistance with the current (blue line) of one of the curves in Fig. 4(a) together with the evolution of the residual function r (orange line). (b) Evolution of the local resistance minima as a function of the degree of oxygen concentration disorder δx_0. (c) Evolution of the local resistance minima as a function of the activation energy E_a.

global oxygen disorder in the sample, respectively. In Fig. 5(a) the red curve shows r as function of the applied current associated with the sample depicting the blue curve response. It can be clearly seen that the initial phase of the electromigration process consists in a homogenization of the oxygen content before a severe disorder sets in at higher currents. A more compelling evidence that the slight improvement of samples' conductivity arises from oxygen concentration ordering comes from Fig. 5(b). In this panel we plot the normalized resistance $R_{\min}(I)/R_{\min}(0)$ for samples with increasing degree of concentration inhomogeneity δx_0. For small values of δx_0 (i.e., rather homogeneous samples), the local minimum is absent, whereas, as δx_0 increases the local minimum becomes progressively more pronounced. This is an interesting finding which could be implemented to quantify the degree of disorder in a sample by measuring the depth of the shallow minima in $R(I)$. Furthermore, the process of current stimulated oxygen ordering should be also influenced by the activation energy barrier to overcome in order to displace the oxygen atoms. In Fig. 5(c) we show that as E_a increases, the ordering is less effective and, consequently, the local minimum becomes shallower. This result seems in agreement with the experimental data shown in Fig. 2 where a higher E_a expected along the a axis exhibits a less-pronounced local minimum.

In an attempt to numerically replicate the oxygen vacancy mappings revealed in Fig. 3, the model must explicitly account for an anisotropic activation energy as described in Sec. II B. The resulting map of oxygen concentration as determined by the numerical simulations with $E_{a_a} = 0.55$ and $E_{a_b} = 0.5$ eV, and reproducing the experimental conditions of Fig. 3, are shown in Fig. 6. Most of the features observed in the optical images of Fig. 3 are also captured by the simulations. In particular, the nucleation of oxygen depleted zones at the location of maximum current crowding and the propagation of an arc-shaped front into the current leads. The lowering of the activation energy along the b direction naturally stimulates oxygen migration along this direction even if the bias current is along a (first row of Fig. 6). Since the current streamlines diverge at the bridge's lower end, the oxygen vacancies migrate preferentially along the direction of the voltage pads and little along the bridge direction. The subsequent anti-EM step further reproduces the experimental findings, namely, a reoxygenation of the previously depleted oxygen vacancy pockets and the formation of new pockets at the bridge's upper

end. The second row of Fig. 6 describes the situation for a 45° rotation of the bridge with respect to the a direction. Although the simulations show stronger effects for the center of the bridge than for the current pads, we do find an asymmetric distribution of oxygen which is explained by an easier diffusion triggered by the current density component J_b with respect to J_a. Finally, the simulation along the b axis (third row of Fig. 6) shows a strong migration almost exclusively along the bridge axis leaving the voltage pads intact.

V. CONCLUSION

In conclusion, we investigated the electromigration process on highly untwinned YBa$_2$Cu$_3$O$_{7-\delta}$ films grown on MgO substrates. We demonstrate that the onset of oxygen migration is determined by the local temperature rather the activation energy associated with the atomic migration. Prior to long-range electromigration, a current amplitude for which the resistivity of the sample decreases is observed. Finite elements modeling suggests that this behavior is caused by a current-stimulated oxygen ordering. The maximum degree of oxygen
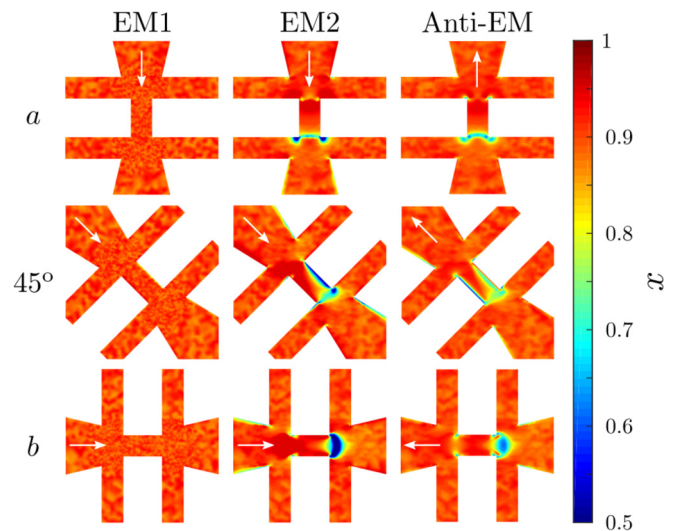

FIG. 6. Numerical simulations reproducing the oxygen vacancy distribution of Fig. 3 using the anisotropic model of Sec. II B with $E_{a_a} = 0.55$, $E_{a_b} = 0.5$ eV.

homogenization being ruled by the initial level of oxygen disorder and the migration activation energy. The numerical model is able to reproduce the observed oxygen vacancy mapping provided that an anisotropic activation energy is taken into account. The proposed model could be further improved by incorporating some degree of twinning, implementing a three-dimensional representation of the $YBa_2Cu_3O_{7-\delta}$ sample, and including a thermomigration term in Eq. (1). These findings provide further understanding on the nonmonotonous change in resistivity systematically observed in oxide samples before severe electromigration.

[1] A. Palau, A. Fernández-Rodríguez, J. C. Gonzalez-Rosillo, X. Granados, M. Coll, B. Bozzo, R. Ortega-Hernandez, J. Suñé, N. Mestres, X. Obradors, and T. Puig, Electrochemical tuning of metal insulator transition and nonvolatile resistive switching in superconducting films, ACS Appl. Mater. Int. **10**, 30522 (2018).

[2] A. S. Dhoot, S. C. Wimbush, T. Benseman, J. L. MacManus-Driscoll, J. R. Cooper, and R. H. Friend, Increased t_c in electrolyte-gated cuprates, Adv. Mater. **22**, 2529 (2010).

[3] L. Bégon-Lours, V. Rouco, A. Sander, J. Trastoy, R. Bernard, E. Jacquet, K. Bouzehouane, S. Fusil, V. Garcia, A. Barthélémy, M. Bibes, J. Santamaría, and J. E. Villegas, High-Temperature-Superconducting Weak Link Defined by the Ferroelectric Field Effect, Phys. Rev. Appl. **7**, 064015 (2017).

[4] P. Gao, Z. Kang, W. Fu, W. Wang, X. Bai, and E. Wang, Electrically driven redox process in cerium oxides, J. Am. Chem. Soc. **132**, 4197 (2010).

[5] E. Robens, R. Rauschen, J. Kaub, J. P. Parras, D. Kemp, C. L. Freeman, and R. A. D. Souza, Perovskite crystal symmetry and oxygen-ion transport: A molecular-dynamics study of perovskite, J. Mater. Chem. A **10**, 2388 (2022).

[6] V. V. Kharton, F. M. Marques, and A. Atkinson, Transport properties of solid oxide electrolyte ceramics: A brief review, Solid State Ionics **174**, 135 (2004).

[7] E. Trabaldo, A. Garibaldi, F. Lombardi, and T. Bauch, Electromigration tuning of the voltage modulation depth in $YBa_2Cu_3O_{7-\delta}$ nanowire-based squids, Supercond. Sci. Techol. **34**, 104001 (2021).

[8] X. D. Baumans, J. Lombardo, J. Brisbois, G. Shaw, V. S. Zharinov, G. He, H. Yu, J. Yuan, B. Zhu, K. Jin, R. B. Kramer, J. V. de Vondel, and A. V. Silhanek, Healing effect of controlled anti-electromigration on conventional and high-T_c superconducting nanowires, Small **13**, 1700384 (2017).

[9] S. Marinković, A. Fernández-Rodríguez, S. Collienne, S. B. Alvarez, S. Melinte, B. Maiorov, G. Rius, X. Granados, N. Mestres, A. Palau, and A. V. Silhanek, Direct visualization of current-stimulated oxygen migration in $YBa_2Cu_3O_{7-\delta}$ thin films, ACS Nano **14**, 11765 (2020).

[10] L. Balcells, L. Peña, R. Galceran, A. Pomar, B. Bozzo, Z. Konstantinovic, F. Sandiumenge, and B. Martinez, Electroresistance and joule heating effects in manganite thin films, J. Appl. Phys. **113**, 073703 (2013).

[11] E. Trabaldo, A. Kalaboukhov, R. Arpaia, E. Wahlberg, F. Lombardi, and T. Bauch, Mapping the Phase Diagram of a $YBa_2Cu_3O_{7-\delta}$ Nanowire Through Electromigration, Phys. Rev. Appl. **17**, 024021 (2022).

[12] R. Arpaia, E. Andersson, A. Kalaboukhov, E. Schröder, E. Trabaldo, R. Ciancio, G. Dražić, P. Orgiani, T. Bauch, and F. Lombardi, Untwinned $YBa_2Cu_3O_{7-\delta}$ thin films on MgO substrates: a platform to study strain effects on the local orders in cuprates, Phys. Rev. Mater. **3**, 114804 (2019).

[13] S. Nawaz, R. Arpaia, F. Lombardi, and T. Bauch, Microwave Response of Superconducting $YBa_2Cu_3O_{7-\delta}$ Nanowire Bridges Sustaining the Critical Depairing Current: Evidence of Josephson-like Behavior, Phys. Rev. Lett. **110**, 167004 (2013).

[14] S. Nawaz, R. Arpaia, T. Bauch, and F. Lombardi, Approaching the theoretical depairing current in $YBa_2Cu_3O_{7-x}$ nanowires, Physica C **495**, 33 (2013).

[15] J. D. Jorgensen, B. W. Veal, A. P. Paulikas, L. J. Nowicki, G. W. Crabtree, H. Claus, and W. K. Kwok, Structural properties of oxygen-deficient $YBa_2Cu_3O_{7-\delta}$, Phys. Rev. B **41**, 1863 (1990).

[16] S. J. Rothman, J. L. Routbort, and J. E. Baker, Tracer diffusion of oxygen in $YBa_2Cu_3O_{7-y}$, Phys. Rev. B **40**, 8852 (1989).

[17] K. Semba and A. Matsuda, Superconductor-to-Insulator Transition and Transport Properties of Underdoped $YBa_2Cu_3O_y$ Crystals, Phys. Rev. Lett. **86**, 496 (2001).

[18] COMSOL AB, Stockholm, Sweden, COMSOLMULTIPHYSICS v.5.4.

[19] M. Nahum, S. Verghese, L. Richards, and K. Char, Thermal boundary resistance for $YBa_2Cu_3O_{7-\delta}$ films, Appl. Phys. Lett. **59**, 2034 (1991).

[20] D. Gupta, W. R. Donaldson, K. Koitkamp, and A. M. Kadin, Optically triggered switching of optically thick YBCO films, IEEE Trans. Appl. Supercond. **3**, 2895 (1993).

[21] A. M. Hofmeister, Thermal diffusivity and thermal conductivity of single-crystal MgO and Al_2O_3 and related compounds as a function of temperature, Phys. Chem. Miner. **41**, 361 (2014).

[22] A. Knizhnik, G. E. Shter, G. S. Grader, G. M. Reisner, and Y. Eckstein, Interrelation of preparation conditions, morphology, chemical reactivity and homogeneity of ceramic YBCO, Physica C **400**, 25 (2003).

[23] I. Grekhov, L. Delimova, I. Liniichuk, A. Lyublinsky, I. Veselovsky, A. Titkov, M. Dunaevsky, and V. Sakharov, Growth mode study of ultrathin HTSCYBCO films on YBaCuNbO buffer, Physica C **324**, 39 (1999).

[24] N. E. Phillips, J. P. Emerson, R. A. Fisher, J. E. Gordon, B. F. Woodfield, and D. A. Wright, Specific heat of $YBa_2Cu_3O_7$, J. Supercond. **7**, 251 (1994).

[25] M. Ikebe, H. Fujishiro, T. Naito, M. Matsukawa, and K. Noto, Anisotropic thermal diffusivity and conductivity of YBCO(123) and YBCO(211) mixed crystals. ii, Jpn. J. Appl. Phys. **33**, 6157 (1994).

[26] S. Collienne, S. Marinković, A. Fernández-Rodríguez, N. Mestres, A. Palau, and A. V. Silhanek, Electrically driven oxygen vacancy aggregation and displacement in $YBa_2Cu_3O_{7-\delta}$ films, Adv. Electron. Mater. **8**, 2101290 (2022).

[27] S. J. Rothman, J. L. Routbort, U. Welp, and J. E. Baker, Anisotropy of oxygen tracer diffusion in single-crystal $YBa_2Cu_3O_{7-\delta}$, Phys. Rev. B **44**, 2326 (1991).

[28] T. A. Friedmann, M. W. Rabin, J. Giapintzakis, J. P. Rice, and D. M. Ginsberg, Direct measurement of the anisotropy of the resistivity in the $a - b$ plane of twin-free, single-crystal, superconducting $YBa_2Cu_3O_{7-\delta}$, Phys. Rev. B **42**, 6217 (1990).

[29] B. H. Moeckly, D. K. Lathrop, and R. A. Buhrman, Electromigration study of oxygen disorder and grain-boundary effects in $YBa_2Cu_3O_{7-\delta}$ thin films, Phys. Rev. B **47**, 400 (1993).

[30] J. Kircher, M. K. Kelly, S. Rashkeev, M. Alouani, D. Fuchs, and M. Cardona, Anisotropy and oxygen-stoichiometry dependence of the dielectric tensor of $YBa_2Cu_3O_{7-\delta}$, Phys. Rev. B **44**, 217 (1991).